Science
AAAS

Supplementary Materials for

Mechanism of siRNA production by a plant Dicer-RNA complex in dicing-competent conformation

Qian Wang *et al.*

Corresponding authors: Sisi Li, liss@szu.edu.cn; Steven E. Jacobsen, jacobsen@ucla.edu; Jiamu Du, dujm@sustech.edu.cn

Science **374**, 1152 (2021)
DOI: 10.1126/science.abl4546

The PDF file includes:

Other Supplementary Material for this manuscript includes the following:

Materials and Methods

Protein expression and purification

The full-length *Arabidopsis thaliana* DCL3 or its mutants were cloned into a self-modified pFastHTB vector to fuse a tandem strep tag to the N-terminus of the target protein. The plasmids were used for generating the bacmids using the *E. coli* strain DH10Bac. The recombinant virus were produced by transfecting the bacmids into the *Spodoptera frugiperda* cell strain SF9 using Cellfectin (Invitrogen). The protein expression employed a Bac-to-Bac baculovirus system in the SF9 cells (Thermo Fisher Scientific). The recombinant expressed proteins were purified using the Strep-Tactin XT® 4Flow beads (IBA Life Science) followed by a MonoQ column (GE Healthcare) and a Superdex G200 column (GE Healthcare). All the RNAs were synthesized at the Takara Company (**Table S1**). To anneal the RNA, the two complement strands were mixed with 1:1 molar ratio, heated in boiling water, and slowly cooled to 4 ˚C.

Cryo-EM sample preparation and data collection

To prepare stable DCL3-RNA complex, the purified DCL3 was mixed with RNA duplex with a molar ratio of 1:2 and further incubated at 4 ˚C for 1 hour. The mixture was crosslinked by 0.1% glutaraldegyde for 10 min on the ice and the reaction was quenched by Tris-HCl, pH 8.0 with a final concentration of 50 mM. The crosslinked DCL3-RNA complex was further purified by a Superdex G200 column (GE Healthcare) with a buffer of 50 mM Tris-HCl, pH 8.0, 100 mM NaCl, 2 mM $CaCl_2$, and

1 mM DTT. The cryo-EM samples of DCL3 in complexes with 40-bp RNA or 30-bp RNA were prepared using 300-mesh Au/Cu R1.2/1.3 grids (Quantifoil, Micro Tools GmbH, Germany), respectively. 4 μl of protein-RNA complex sample at a concentration of ~ 1.8 mg/ml was loaded on the grid which were pre-glow discharged by Plasma cleaner (PDC-32G, Harrick plasma) for 30 seconds at medium power setting. The grids were blotted for 3 s by the blotting filter paper (GE Healthcare Life Sciences) after waiting for 5 s in the condition of 8 °C and 100% humidity and then plunged into liquid ethane cooled by liquid nitrogen using Vitrobot (Mark IV, Thermo Fisher Scientific) .

For the DCL3-40-bp-RNA complex, the micrographs were collected on a Titan Krios microscope (#5, Futian) at 300 kV equipped with a K3 Summit direct electron detector (Gatan). Images were recorded using the program SerialEM (*31*) at a nominal magnification of 105,000 x in super-resolution mode. The pixel size was 1.1 Å/pixel and the defocus range were set from -1.7 μm to -2.5 μm. The electron exposure on the detector was about 50 $e^-/Å^2$. Each micrograph stack contains 32 frames, obtaining 3,731 micrographs in total. For the DCL3-30-bp-RNA complex, the micrographs were collected on a Titan Krios microscope (#1, Baoan) at 300 kV equipped with a K2 Summit direct electron detector (Gatan). Images were recorded using the program SerialEM (*31*) at a nominal magnification of 165,000 x in super-resolution mode. The pixel size was 0.84 Å/pixel and the defocus range were set from -2.5 μm to -3.5 μm.

The electron exposure on the detector was about 50 $e^{-}/Å^{2}$. Each micrograph stack contains 32 frames, obtaining 3,925 micrographs in total. All the necessary parameters for data collecting are list in **Table S2.**

Structure determination

Total 3,576 movies were used for the DCL3-40-bp-RNA complex. All frames of the movie were aligned, dose-weighted, and summed to produce average micrographs, each micrograph was corrected from motion with a sub-region motion correction of 5 x 5 patches and dose-weighting by USCF MotionCor2 (*32*). CTFFIND 4.1 (*33*) was used to calculate the contrast transfer function (CTF) parameter and produce the CTF power spectrum on basis of summed micrographs from MotionCor2 for all micrographs with dose-weighting. 2,199,032 particles were auto-picked from 3,576 micrographs using Relion 3.1 (*34*). After 2D classification, 1,763,534 particles were selected to the first 3D classification. After 50 iterations of 3D classification, we finally obtained 220,948 particles for 3D auto-refinement with *C*1 symmetry. The soft mask was performed to improve the local resolution of our density map. Model building was carried our directly using the 3.1 Å cryo-EM map using the program Coot (*35*). The RNA duplex was readily built into the map. The protein part was manually built with the guidance of the homology domain structures of human Dicer (PDB code: 5ZAM) or Giadia Dicers (PDB code: 2FFL) (*3*, *6*).

2,793 movies were used for DCL3-30-bp-RNA complex data processing in Relion 3.06 (*36*). The CTF parameters were estimated using the program Gctf (*37*). The data processing procedure was similar to that of DCL3-40-bp-RNA complex. Briefly, 877,627 particles were selected from 2D classes. 228,073 particles were used for further 3D classification. 155,929 good particles were selected to 3D auto-refinement. To improve the resolution, we performed CTF refinement, which yielded a map at 3.73 Å resolution for model building. The model building was conducted using the program Coot (*35*) with the DCL3-40-bp-RNA complex structure as a reference.

The overall models were subjected to global refinement and minimization in real_space_refinement using Phenix with the rotamer restraints and Ramachandran restraints (*38*). All the figures were created in PyMOL (Schrödinger) and Chimera (*39*).

All reported resolutions are based on the gold-standard FSC = 0.143 criteria (*40*), and the final FSC curve were corrected for the effect of a soft mask using high-resolution noise substitution. The local resolution map was calculated using ResMap (*41*).

***In vitro* dicing assay**

All of the dicing assay were performed in a reaction buffer of 50 mM HEPES-KOH, pH 8.0, 150 mM NaCl, 5 mM $MgCl_2$, and 2 mM DTT. Generally, the cleavage assay was performed by mixing 0.003 nmol protein and 0.01 nmol substrate RNA in a 50 μl reaction system at 37 ˚C for 5 min, 40 min, and 2 min, respectively, according to the

purpose. A 30-bp TAS1a derived dsRNA with the 5'-phopsohrylation in guide strand and 1-nt 3'-overhang in complementary strand was used as standard RNA substrate (**Table S1**). To test influence of the overhang length, the same 30-bp TAS1a derived RNAs but with longer 3'-overhanging C in complementary strand were used as RNA substrate (**Table S1**). To confirm the complete loss of the dicing activity of one strand but keeping the activity towards the other strand and to show the completely cutting state, the dicing assays for D1316A/E1319A/E1224A/D1228A mutant, D1133A/E1136A/E1015A/D1019A mutant, and a wild type sample were carried out with the same reaction condition, but 8 folds more proteins were used. The reaction was quenched by adding equal amount of 2 x RNA denaturing loading buffer and heated at 95 ˚C for 3 min. Cleavage products were loaded to 15~20% denaturing PAGE and electrophoresis at a constant power of 5 W in 3.5 hours on a High voltage electrophoresis system (BIO-RAD). The gel was stained by the SYBR® Gold Nucleic Acid Gel Stain (Invitrogen) and visualized on an Ultra-sensitive Multi-function Imager (GE Healthcare). All reactions were done in triplicate. The quantification of the gel bands was performed using the software ImageJ. The data were analyzed by the program Origin 7.0 (http://www.originlab.com) with two-tailed Student's t-test. The conventions used to report the statistical significances of $p<0.05$, $p<0.01$, $p<0.001$, and $p<0.0001$ are denoted by *, **, ***, and ****, respectively.

Cloning for functional studies

Full length wild type DCL3 (DCL3 WT) was amplified from genomic DNA with Primer 1/2 (**Table S1**) including ~0.65 kb upstream of its start codon, and cloned into pENTR/D-TOPO (Thermo Fisher). All mutant forms of DCL3 were generated based on this DCL3 WT with a PCR based method using the primers listed in **Table S1**. DCL3 WT and mutants were all subcloned into a plant expression binary vector pEG302 with a C-terminal 3 x FLAG tag, using LR clonase (Invitrogen).

Plant material and growth conditions

Arabidopsis thaliana were grown under standard greenhouse conditions with approximately 16h light/8h dark cycles at 22 ˚C. Transgenic *dcl234* (*9*) expressing DCL3 WT or mutants were generated by *Agrobacterium tumefaciens* AGL0 mediated transformation. T1 transformants were selected based on hygromycin resistance.

Western blot

Four week old leaf tissues were ground in liquid nitrogen, resuspended in 5x Laemmli buffer and incubated at 95 ˚C for 5 min. The boiled samples were centrifuged at top speed for 5 min. Supernatant was subject SDS-PAGE (Invitrogen) and subsequently transferred onto PVDF membrane in Towbin buffer at 80 V for 90 min. After blocking with 5% skim milk, the membrane was incubated with HRP conjugated anti-FLAG M2 antibody (Sigma A8592) overnight at 4 ˚C with gentle shaking. The signals were detected with ECL prime western blotting detection reagent (Amersham).

Small RNA sequencing

Six- to eight-week-old floral tissues of two independent T1 plants of each genotype were used to characterize the abundance of 24 nt siRNA. Total RNA was extracted using the Direct-zol RNA Miniprep kit (Zymo) according to the manufacturer's instructions. Two micrograms of total RNA was mixed with equal volume of the 2x RNA loading dye (NEB), denatured at 65°C for 10 min and immediately chilled on ice. Denatured total RNA was separated on 15% TBE urea gel (Invitrogen) and small RNAs from 15-30 nts were excised. The excised gel pieces were forced through gel breaker tubes (IST engineering inc) by centrifuging at 20,000 g for 3 min. small RNA was then eluted with nuclease free water by incubation at 70°C for 10 min and precipitated with EtOH. Small RNA libraries were made using NEBNext® Small RNA Library Prep Set for Illumina® (Multiplex Compatible) (NEB) according to the manufacturer's instructions.

Small RNA-seq analysis.

Small RNA reads adaptor were removed with TrimGalore (v0.4.2, https://github.com/FelixKrueger/TrimGalore) and mapped to *Arabidopsis thaliana* reference genome TAIR10 using Bowtie2 (v2.1.0) allowing only uniquely mapping reads with 0 mismatches (*42*). sRNA reads that mapped to chloroplast, mitochondrial DNA, tRNA, rRNA, small nucleolar RNAs (snoRNAs), and small nuclear RNAs (snRNAs) were removed using bedtools (v2.26.0) (*43*). Pol IV dependent small RNA producing regions were defined from previous publications (*23*). Total miRNA amount

was obtained by counting all 21-nt sRNA over miRNA producing regions as previously defined (*44*). .

Figures

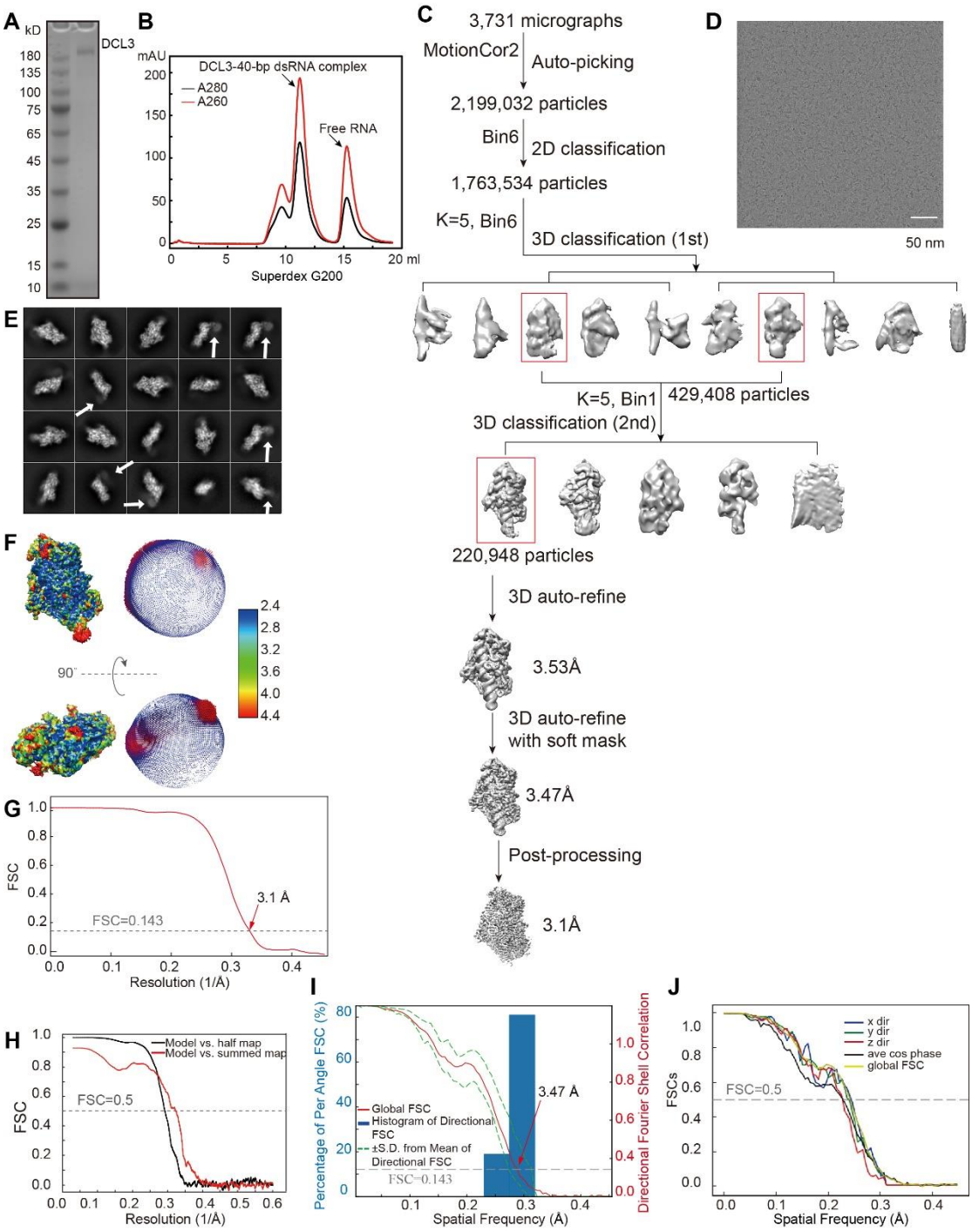

Fig. S1. Cryo-EM structural analysis of DCL3 in complex with a 40-bp pre-siRNA possessing 5'-phosphorylated-A1 on guide strand and 1-nt 3'-overhang on complementary strand. A. The SDS-PAGE of the purified DCL3 showing the purity of the protein sample. **B.** The gel-filtration profile for the DCL3-40-bp RNA complex. **C.** Flowchart for cryo-EM data processing. **D.** Representative cryo-EM micrograph. **E.**

2D class average of the DCL3-40-bp-dsRNA complex. The arrows indicate the faint density for the helicase domain which was too weak to be modeled. **F.** Local resolution map of the DCL3-40-bp-dsRNA complex and angular distribution of particles for the final 3D reconstruction in two orientations related by 90°. **G.** Gold standard FSC curves for DCL3-40-bp-dsRNA complex 3D reconstruction by Relion. **H.** The FSC calculated between the refined structure and the half map used for refinement (black), and the full map (red). **I-J**. Global FSC (**I**) and the directional FSC (**J**) of the DCL3-40-bp-dsRNA complex in the last iteration of the 3D auto-refinement by the website of https://3dfsc.salk.edu (*45*).

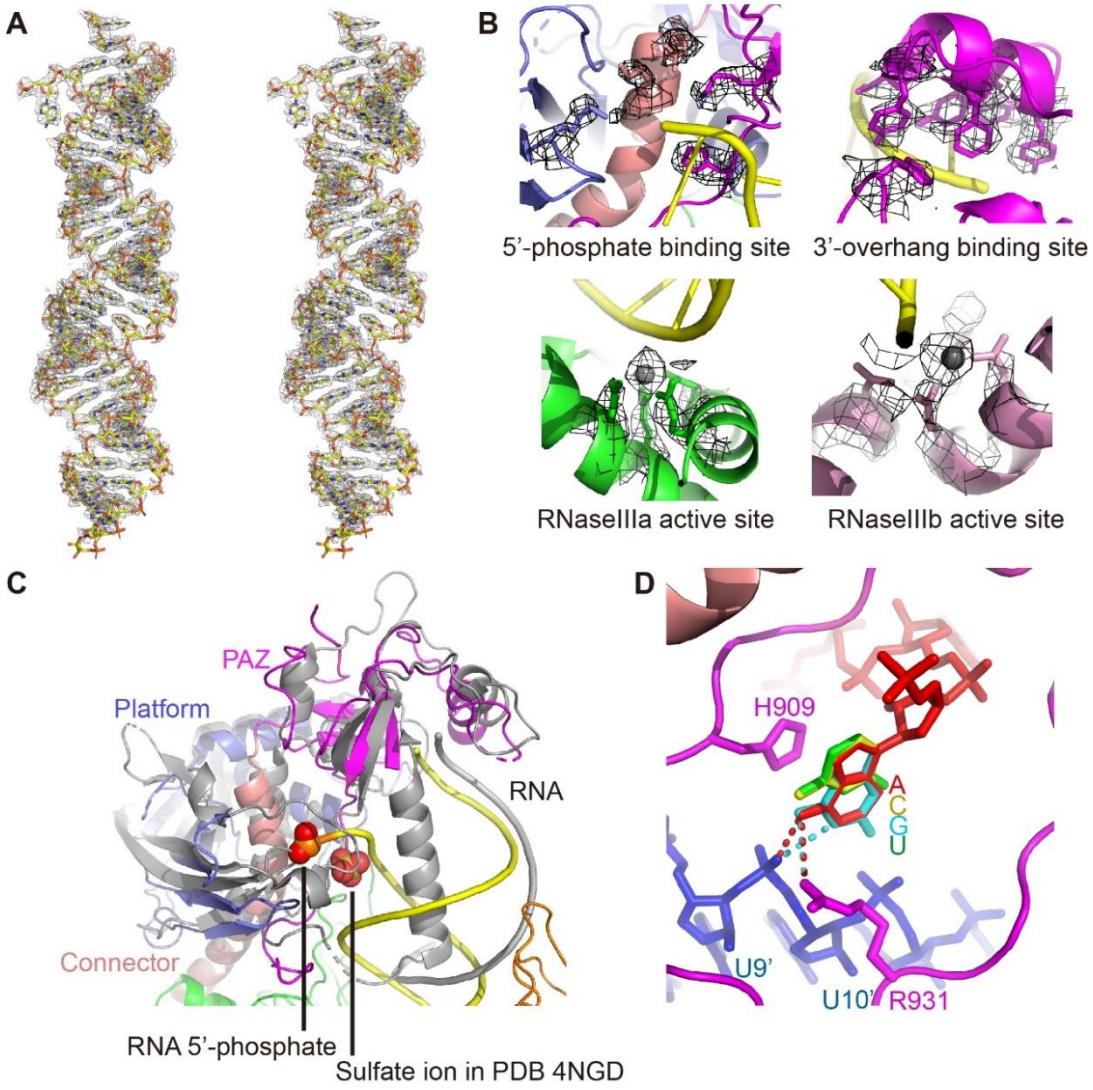

Fig. S2. The cryo-EM density and recognition of 5'-phosphorylated-A1. A. A stereo view of the cryo-EM density map of the 40-bp pre-siRNA. **B.** The representative cryo-EM map for some residues and the Ca^{2+} ions in the 5'-phosphate binding site (upper left), the 3'-overhang binding site (upper right), the RNaseIIIa active site (lower left), and the RNaseIIIb active site (lower right) showed that most of the RNA interacting key residues possess good electron density. **C.** The superimposition of the platform-PAZ-connector cassette of DCL3-RNA complex (in color) and human Dicer (in silver, PDB code: 4NGD). The 5'-phosphate group of the guide strand RNA in this research and the sulfate ion supposed to mimic 5'-phosphate group in the human Dicer platform-PAZ-connector-RNA structure were highlighted in space-filling, respectively, positioning 5'-phosphate binding pockets of both DCL3 and human Dicer in the same pockets. **D.** The 5'-A1 (in red) is specifically recognized by the stacking and hydrogen bonding interactions. The modeling of 5'-A1 (in red) to C (in yellow), G (in cyan), and U (in green) shows that C and U are too small to form the same intermolecular interactions.

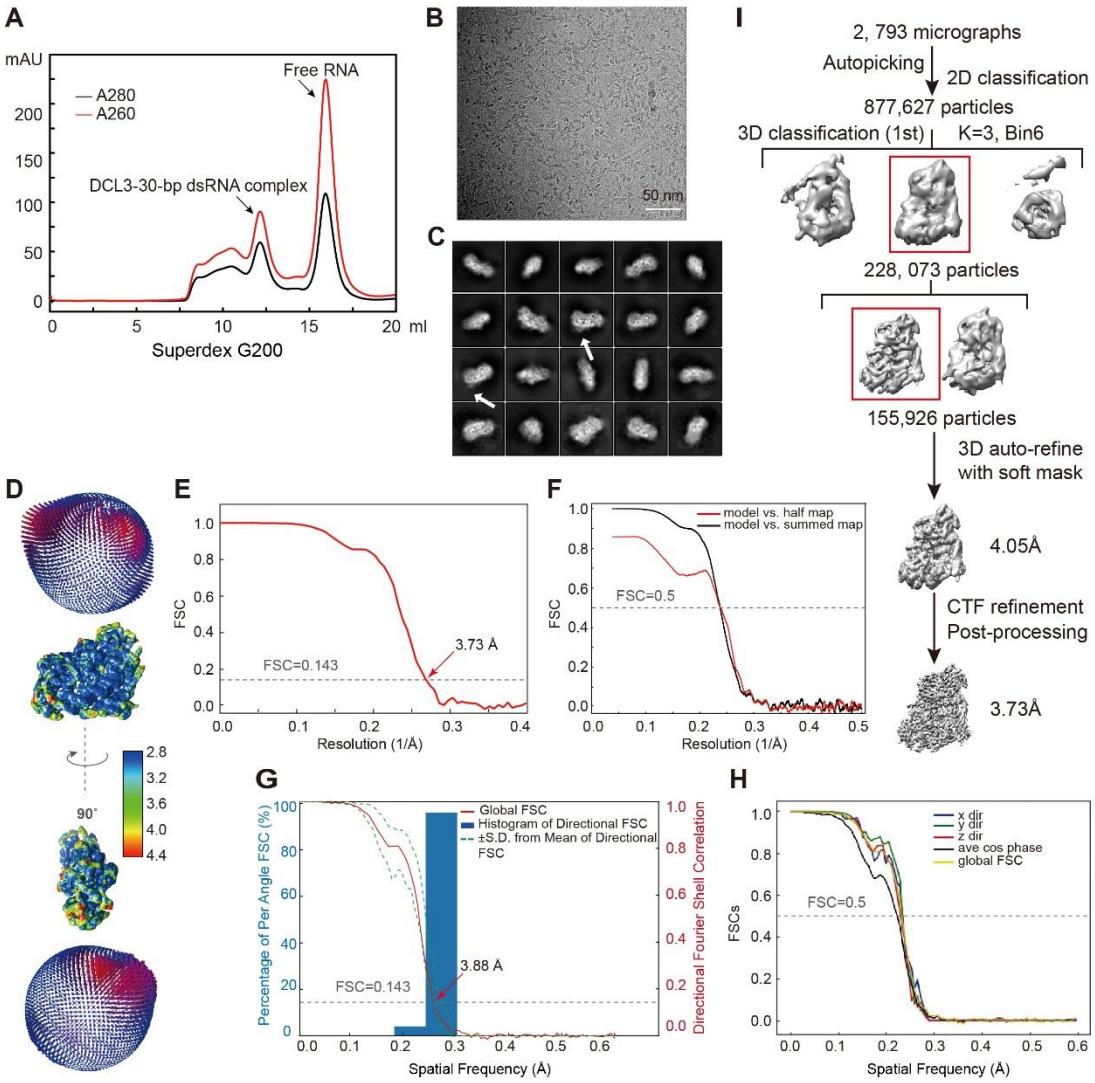

Fig. S3. Cryo-EM structural analysis of DCL3 in complex with a 30-bp pre-siRNA possessing 5'-phosphorylated-U1 on the guide strand and 2-nt 3'-overhang on the complementary strand. A. The gel-filtration purification profile for the DCL3-30-bp dsRNA complex. **B.** Representative cryo-EM micrograph. **C.** 2D class averages of the DCL3-30-bp-dsRNA complex. The arrows indicate the faint density for the helicase domain which is too weak to be modeled. **D.** Local resolution map of the DCL3-30-bp-dsRNA complex and angular distribution of particles for the final 3D reconstruction in two orientations related by 90°. **E.** Calculated FSC curve of the final 3D reconstruction of DCL3-30-bp-dsRNA complex after post-processing in Relion. **F.** The FSC calculated between the refined structure and the half map used for refinement (black), and the full map (red). **G-H.** Global FSC (**G**) and the directional FSC (**H**) of the DCL3-30-bp-dsRNA complex in the last iteration of the 3D auto-refinement by the website of https://3dfsc.salk.edu (*45*). **I.** Flowchart for cryo-EM data processing.

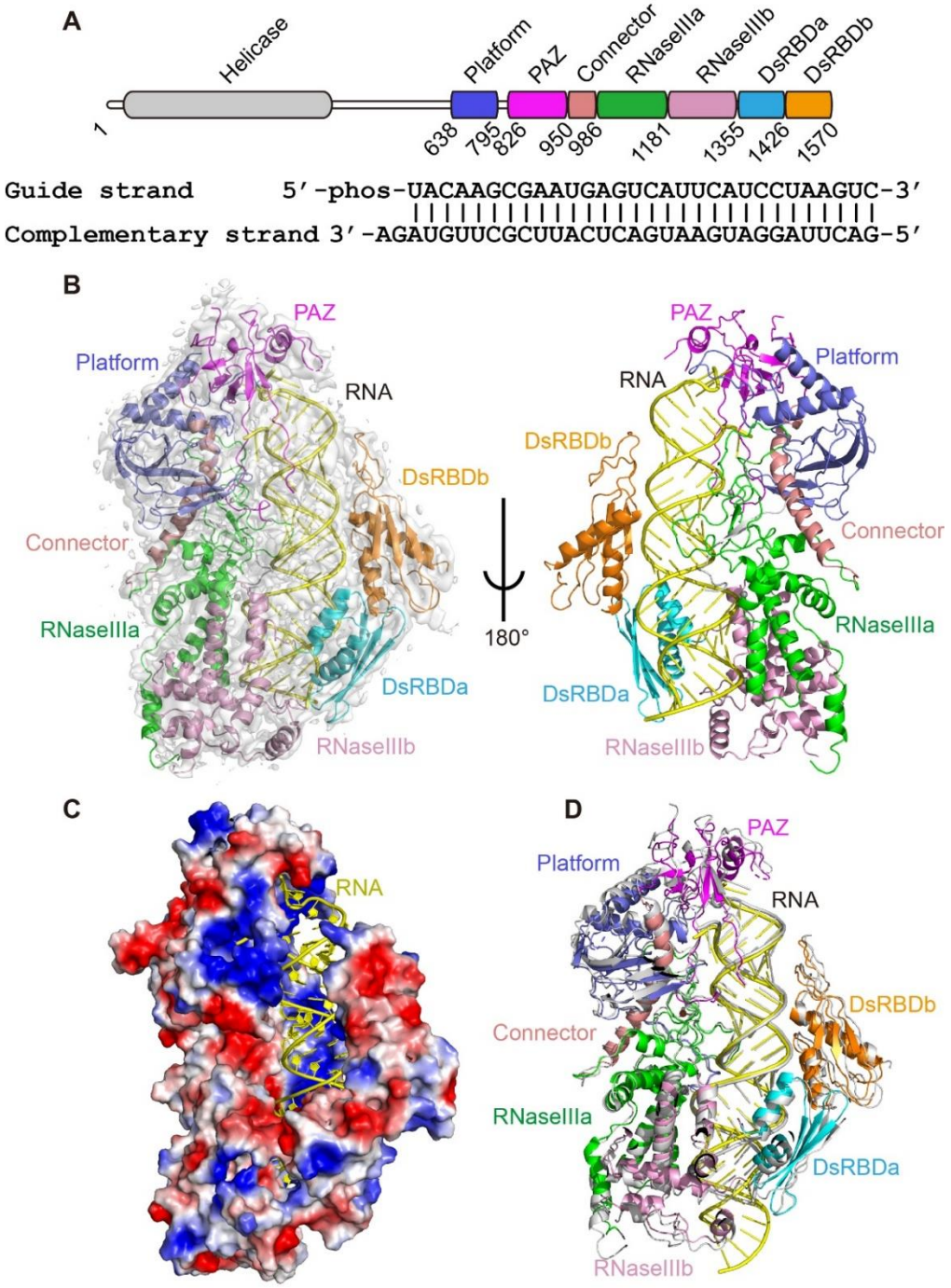

Fig. S4. Overall structure of DCL3 in complex with a 30-bp pre-siRNA possessing 5'-phosphorylated-U1 on the guide strand and 2-nt 3'-overhang on the complementary strand. A. The domain architecture of DCL3 and the RNA sequence used for structure determination. **B.** The overall structure of DCL3 in complex with a 30-bp pre-siRNA. The cryo-EM density map was overlaid on the left panel. **C.** An electrostatic surface view of DCL3 showing the RNA is captured within a highly positively charged RNA binding channel. **D.** The superimposition of DCL3 in complex with 40-bp pre-siRNA (in color) and 30-bp pre-siRNA (in silver) showing almost identical conformations.

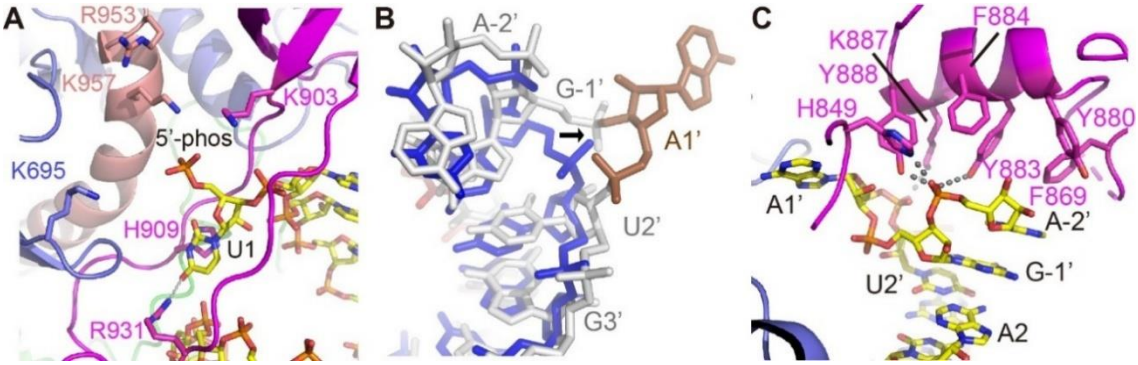

Fig. S5. Recognition of the 30-bp RNA. A. The 5'-phosphate group of guide strand of the 30-bp RNA anchors into the same positively charged pocket. The U1 base stacks with H909 and forms a hydrogen bond with R931, but no direct hydrogen bonding interaction with the complementary strand as in the case of the adenine base. **B.** A stick view of the superimposition of the complementary strands of 3'-1-nt overhang (in blue) and 3'-2-nt overhang (in silver, with the flipped out A1' highlighted in brown) showing the molecular details for RNA flipping and folding back. **C.** Despite the longer overhang, the 3'-end of the complementary strand of 2-nt overhang RNA is anchored by the PAZ domain aromatic cap, resembling the interaction of 1-nt overhang RNA.

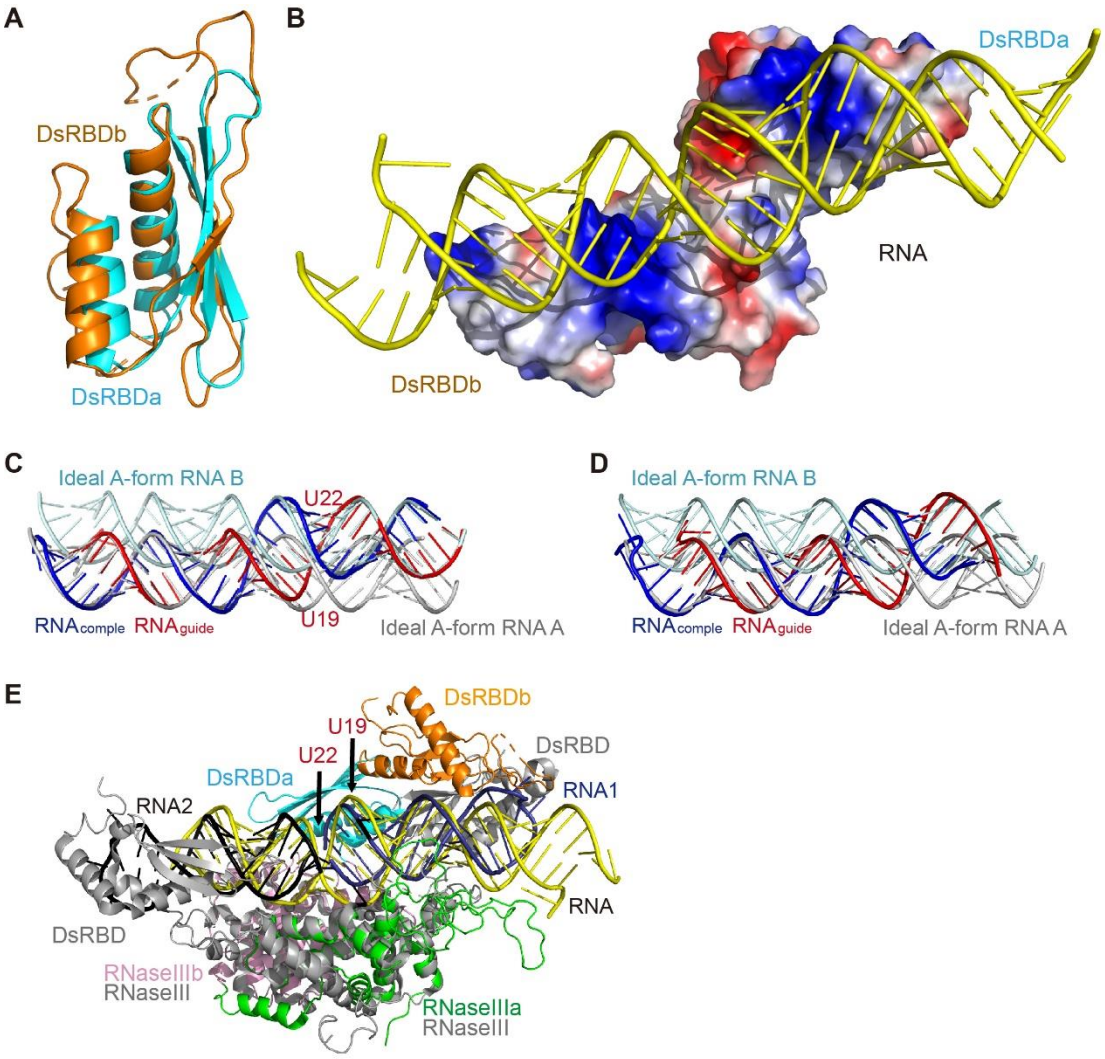

Fig. S6. The conformation of dsRBDa/b, RNA conformational change, and comparison with yeast Rnt1p. A. The superimposition of the dsRBDa (in cyan) and dsRBDb (in orange) domains showing that they adopt very similar folds and conformations. **B.** The two dsRBDs use their highly positively charged interface to bind to RNA backbone. **C-D.** The 5'-half and 3'-half of either the 40-bp pre-siRNA (**C**) or the 30-bp pre-siRNA (**D**) aligned well to the ideal A-form RNA (in pale cyan and in silver) in parallel. The middle region of RNA, marked from U19 to U22 of the guide strand, undergoes a conformation change. **E.** The superimposition of DCL3-RNA complex (in color) and yeast RNaseIII Rnt1p-RNA complex (protein in silver, RNAs in black and dark blue, respectively, PDB code: 5T16) showed that the arrangement of DCL3 RNaseIIIa/b resembles the Rnt1p RNaseIII homodimer, and the RNA conformation change observed in DLC3-RNA complex mirrors the RNA alignment shift in the Rnt1p-RNA complex. In contrast, the two dsRBDs of Rnt1p dimer occupy different positions from the DCL3 dsRBDa/b, suggesting a dynamic RNA-binding feature of the dsRBD in the dicing process.

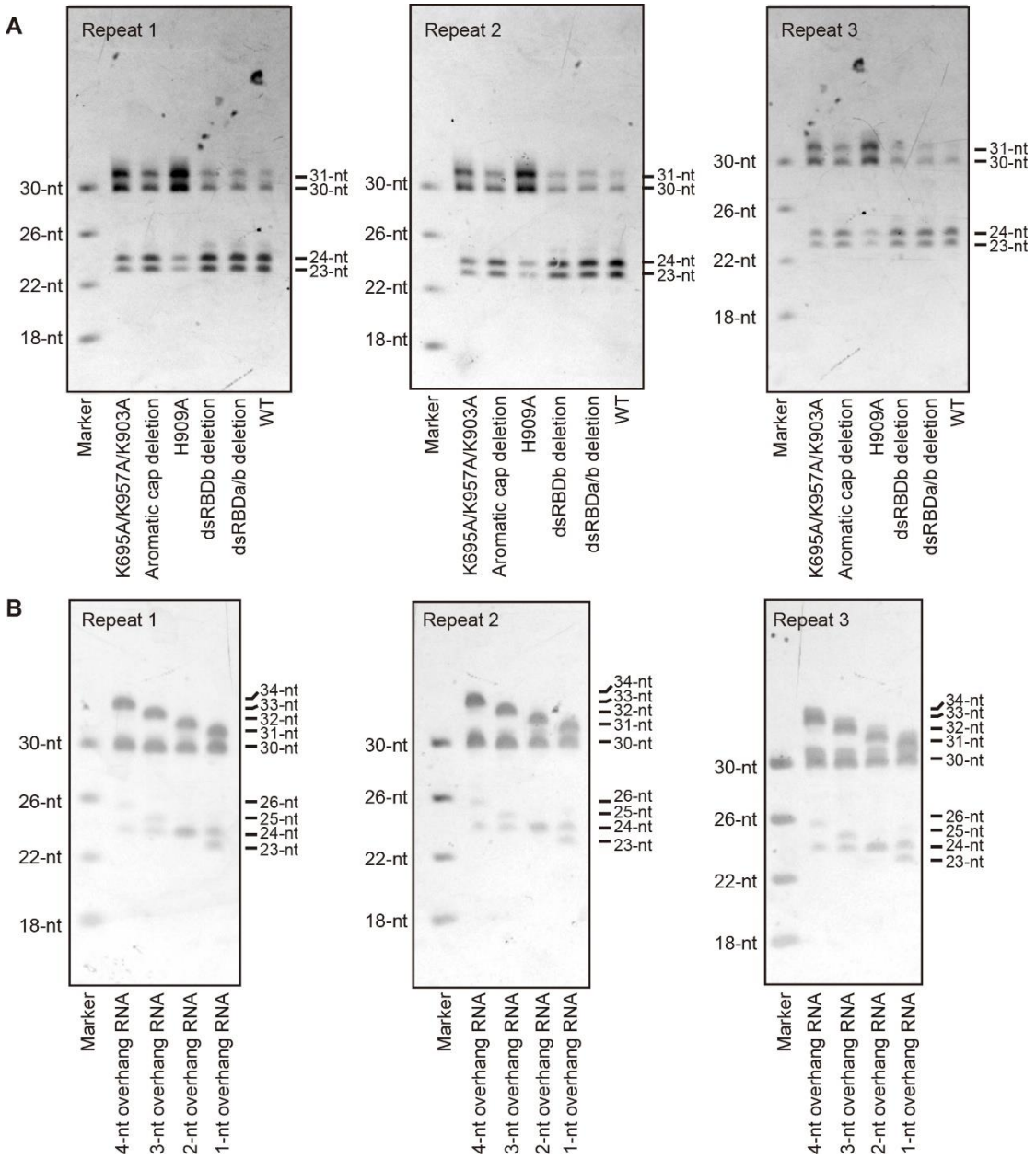

Fig. S7. The *in vitro* dicing assay. A. Gels of the three repeats of the *in vitro* dicing assay of DCL3 and its mutants with a 30-bp RNA substrate possessing 5'-phophorylated-A1 on the guide strand and 1-nt 3'-overhang on the complementary strand. Aromatic cap deletion, Δ865-895; dsRDBb deletion, Δ1450-1570; dsRBDa/b deletion, Δ1356-1570. **B.** Gels of the three repeats of the *in vitro* dicing activity of DCL3 against different RNAs with the same guide strand possessing 5'-phophorylated-A1 and various complementary strands with different 3'-overhang lengths.

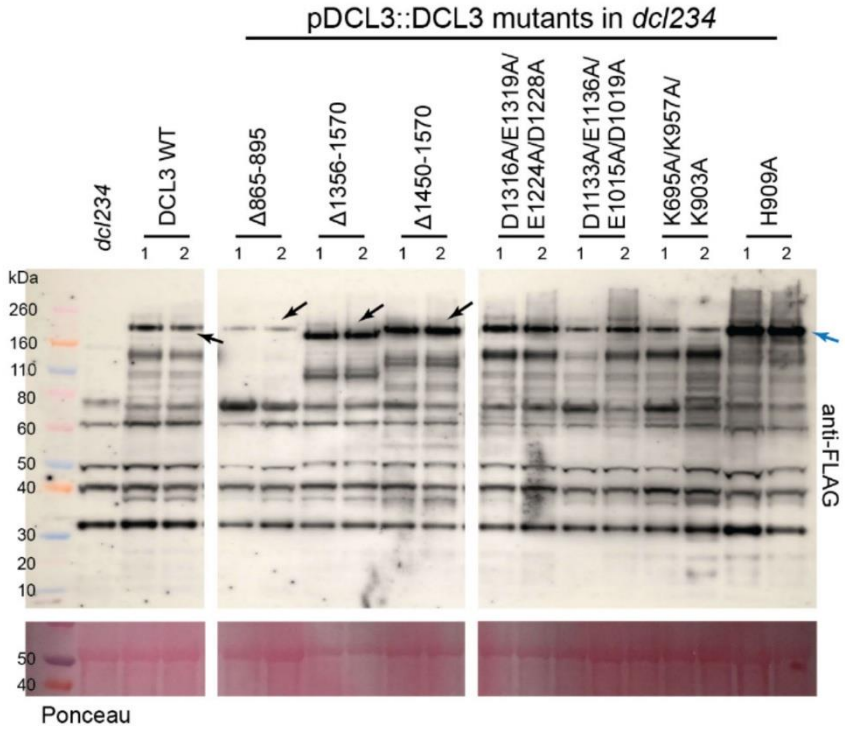

Fig. S8. A Western blot showing the expression levels of DCL3 variants in the transgenic plants used for the generation of sRNA libraries. The images are from the same blot. Black arrows indicate the expected sizes of DCL3 WT and corresponding deletion mutants. Blue arrow indicates the size of all amino acid substitution mutants.

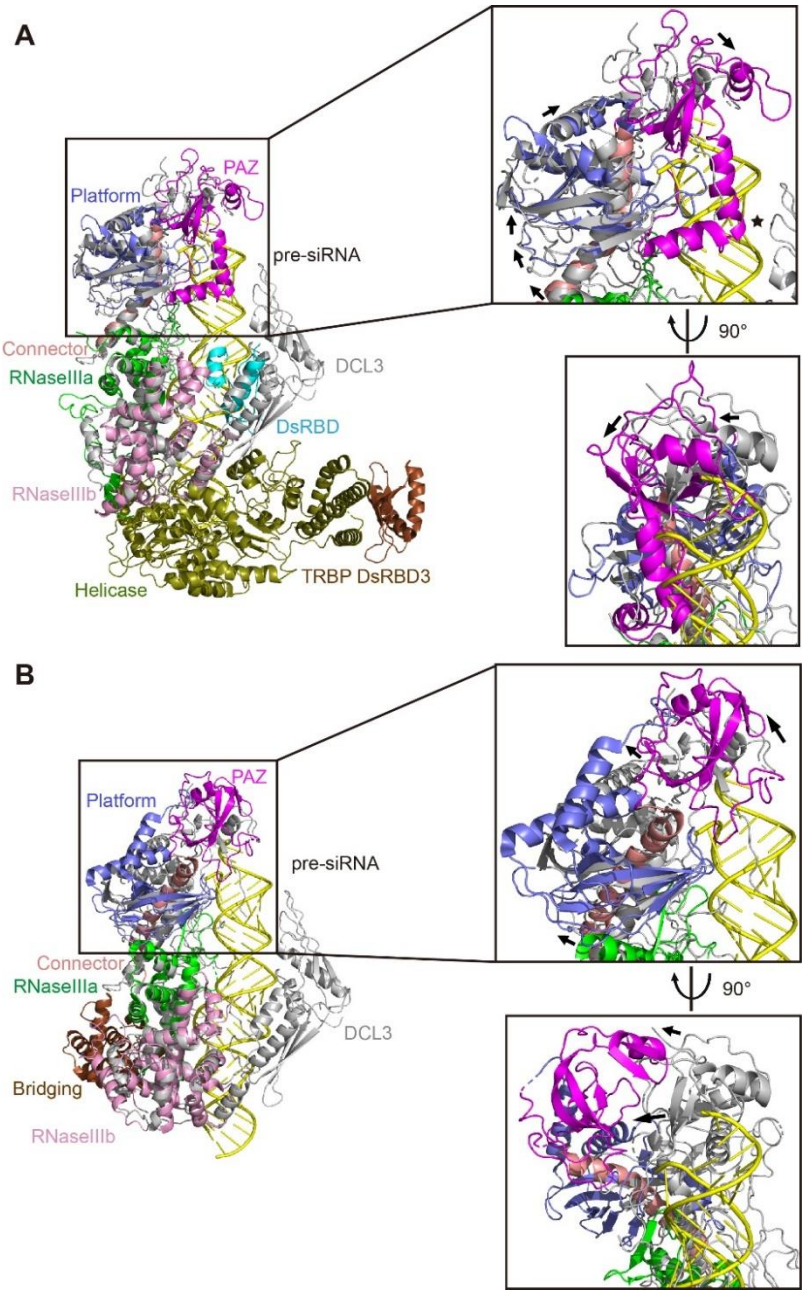

Fig. S9. The structural comparison of different Dicers reveals the potential molecular mechanism for RNA length measurement. The superimpositions of DCL3 (in silver) and human Dicer (**A,** PDB code: 5ZAM, in color) or *Giardia* Dicer (**B,** PDB code: 2FFL, in color) based on their positions of RNaseIIIa/b domains are shown in left panels. The RNA from DCL3-RNA complex is highlighted in yellow to represent the active dicing conformation RNA. Enlarged views of the platform-PAZ-connector cassette are shown in two orientations related by 90° in right panels**.** The directions of the conformational changes from DCL3 to other Dicers are shown by arrows. **A.** Human Dicer intends to form more compact conformation relative to DCL3, consistent with its shorter product. **B.** *Giardia* Dicer intends to move away from the RNA-end, consistent of its longer product.

Table S1 Oligos used in this research

Name	Sequence	Purpose
DNA		
pDCL3 F	CACCCCGACCGAAATCCTCATGACCTAA	Primer
gDCL3 R	CTTTTGTATTATGACGATCTTGCGGCGC	Primer
HTB-DCL3-F	CGTCCCACCATCGGGCGCGGATCCATGTGGAGCCACCCGCAGTT	Primer
HTB-DCL3-R	AAGCTTGGTACCGCATGCCTCGAGCTACTTTTGTATTATGACGATC	Primer
Δ865-895 F	AACCAGCCGTTGATGAAGTTGA	Primer
Δ865-895 R	AGAAGAATCGCTTACGGCTTCA	Primer
Δ1356-1570 F	TAGCTCGAGGCATGCGGTACCAA	Primer
Δ1356-1570 R	AAGCTGAAGTTTATCTGGAGTTACAAGTG	Primer
Δ1450-1570 F	TAGCTCGAGGCATGCGGTACCAA	Primer
Δ1450-1570 R	TCTGTCGCTATGATTGCAAGCAAGA	Primer
K695A F	CTTTACTTGGTCAGGGCTCTTGTCAAGG	Primer
K695A R	AGCCCTGACCAAGTAAAGGTCCATCTCA	Primer
K903A F	CCGTTGATGAAGTTGGCTCAGAGTCACC	Primer
K903A R	AGCCAACTTCATCAACGGCTGGTTCGGG	Primer
K957A F	CCGCGTGCTGTGCTAGCTTCAATCTACT	Primer
K957A R	AGCTAGCACAGCACGCGGTACATCAATT	Primer
H909A F	CAGAGTCACCATGCGGCTAACCTTTTAG	Primer
H909A R	AGCCGCATGGTGACTCTGCTTCAACTTC	Primer
D1133A F	TCAAAATCTGTATCAGCTTGCGCTGAGG	Primer
D1133A R	GCTGATACAGATTTTGAAACTACCCATC	Primer
E1136A F	GTATCAGCTTGCGCTGCTGCCCTGATTG	Primer
E1136A R	AGCAGCGCAAGCTGATACAGATTTTGAA	Primer
E1015A F	TCAATGGAGCGGTTGGCTCTGCTCGGGG	Primer
E1015A R	AGCCAACCGCTCCATTGAAAATGATTCG	Primer
D1019A F	TTGGCTCTGCTCGGGGCTTCAGTCTTGA	Primer
D1019A R	GCCCCGAGCAGAGCCAACCGCTCCATTG	Primer
D1316A F	CCTAAGGCTCTTGGAGCTGTTGTGGAGA	Primer
D1316A R	GCTCCAAGAGCCTTAGGGCCCTGTATTG	Primer

E1319A F	CTTGGAGCTGTTGTGGCTAGTATCGCTG	Primer
E1319A R	AGCCACAACAGCTCCAAGAGCCTTAGGG	Primer
E1224A F	TCATACGAGAGATTAGCTTTTCTTGGCG	Primer
E1224A R	AGCTAATCTCTCGTATGAATAGGATTCA	Primer
D1228A F	TTAGCTTTTCTTGGCGCTTCTGTACTGG	Primer
D1228A R	GCGCCAAGAAAAGCTAATCTCTCGTATG	Primer
RNA		
TAS1a F 40-ph-A	5’-phos-AACAAGCGAAUGAGUCAUUCAUCCUAAGUCUGCAUAAAGU	EM-structure
TAS1a R 40-1-overhang	ACUUUAUGCAGACUUAGGAUGAAUGACUCAUUCGCUUGUUC	EM-structure
TAS1a F 30-ph-U	5’-phos-UACAAGCGAAUGAGUCAUUCAUCCUAAGUC	EM-structure
TAS1a R 30-2-overhang	GACUUAGGAUGAAUGACUCAUUCGCUUGUAGA	EM-structure
TAS1a F 30-ph-A	5’-phos-AACAAGCGAAUGAGUCAUUCAUCCUAAGUC	Dicing assay
TAS1a R 30-1-overhang	GACUUAGGAUGAAUGACUCAUUCGCUUGUUC	Dicing assay
TAS1a R 30-2-overhang	GACUUAGGAUGAAUGACUCAUUCGCUUGUUCC	Dicing assay
TAS1a R 30-3-overhang	GACUUAGGAUGAAUGACUCAUUCGCUUGUUCCC	Dicing assay
TAS1a R 30-4-overhang	GACUUAGGAUGAAUGACUCAUUCGCUUGUUCCCC	Dicing assay

Table S2. Cryo-EM data collection, refinement, and validation statistics

	AtDCL3-40bp-dsRNA	AtDCL3-30bp-dsRNA
EMDB code	EMD-31963	EMD-31964
PDB code	7VG2	7VG3
Data collection and processing		
Microscopy	Titan Krios (#5, Futian)	Titan Krios (#1, Baoan)
Voltage (kV)	300	300
Camera	Gatan K3 Summit	Gatan K2 Summit
Magnification	105,000	165,000
Pixel size (Å/pixel)	1.1	0.84
Total electron exposure ($e^-/Å^2$)	50	50
Exposure rate ($e^-/A^2/sec$)	20	8
Number of frames per movie (no.)	32	32
Defocus range (μm)	-1.7 to -2.5	-2.5 to -3.5
Automation software	SerialEM	SerialEM
Energy filter slit width (eV)	20	20
Micrographs collected (no.)	3,731	3,925
Micrographs used (no.)	3,576	2,793
Total extracted particles (no.)	2, 199, 032	877, 627
For each reconstruction		
Refined particles (no.)	220,948	155,929
Final particles (no.)	220,948	155,929
Data processing software	Relion3.1	Relion3.0.6
Point group	*C*1	*C*1
Resolution (global, Å)		
FSC 0.143 (unmasked/masked)	3.47/3.1	4.02/3.73
FSC 0.5 (unmasked/masked)	4.13/3.41	4.42/4.20
Local resolution range (Å)	2.4-4.4	2.8-4.4
Map sharpening B factor ($Å^2$)	-121	-253
Map sharpening methods	Half-maps correlation	Half-maps correlation
Refinement		
Refinement package	Phenix	Phenix
- real or reciprocal space	Real space	Real space
- resolution cutoff (Å)	3.1	3.73
Model-Map scores		
- CC	0.79	0.84
No. atoms	8,203	8,111
Protein / RNA	6,695 / 1,505	6,793 / 1,315
Ca^{2+} / Zn^{2+}	2 / 1	2 / 1
B-factors ($Å^2$)	41.1	62.9
Protein / RNA	40.8 / 42.8	63.6 / 59.0
Ca^{2+} / Zn^{2+}	27.8 / 49.8	47.0 / 63.4
R.m.s. deviations		
Bond lengths (Å)	0.017	0.005
Bond angles (°)	1.489	1.024
Validation		
MolProbity score	2.67	1.98
Clashscore	13.86	4.24
Poor rotamers (%)	4.94	1.72

C-beta outlier (%)	0.12	0.25
CaBLAM outliers	3.94	6.49
EMRinger score	3.82	3.10
Ramachandran plot[b]		
Favored (%)	91.9	87.9
Allowed (%)	7.9	11.6
Outlier (%)	0.2	0.5

References and notes

1. V. N. Kim, J. Han, M. C. Siomi, Biogenesis of small RNAs in animals. *Nat. Rev. Mol. Cell Biol.* **10**, 126–139 (2009). doi:10.1038/nrm2632 Medline

2. G. Meister, Argonaute proteins: Functional insights and emerging roles. *Nat. Rev. Genet.* **14**, 447–459 (2013). doi:10.1038/nrg3462 Medline

3. I. J. Macrae, K. Zhou, F. Li, A. Repic, A. N. Brooks, W. Z. Cande, P. D. Adams, J. A. Doudna, Structural basis for double-stranded RNA processing by Dicer. *Science* **311**, 195–198 (2006). doi:10.1126/science.1121638 Medline

4. Y. Tian, D. K. Simanshu, J.-B. Ma, J.-E. Park, I. Heo, V. N. Kim, D. J. Patel, A phosphate-binding pocket within the platform-PAZ-connector helix cassette of human Dicer. *Mol. Cell* **53**, 606–616 (2014). doi:10.1016/j.molcel.2014.01.003 Medline

5. J. E. Park, I. Heo, Y. Tian, D. K. Simanshu, H. Chang, D. Jee, D. J. Patel, V. N. Kim, Dicer recognizes the 5′ end of RNA for efficient and accurate processing. *Nature* **475**, 201–205 (2011). doi:10.1038/nature10198 Medline

6. Z. Liu, J. Wang, H. Cheng, X. Ke, L. Sun, Q. C. Zhang, H.-W. Wang, Cryo-EM structure of human Dicer and its complexes with a pre-miRNA substrate. *Cell* **173**, 1191–1203.e12 (2018). doi:10.1016/j.cell.2018.03.080 Medline

7. N. K. Sinha, J. Iwasa, P. S. Shen, B. L. Bass, Dicer uses distinct modules for recognizing dsRNA termini. *Science* **359**, 329–334 (2018). doi:10.1126/science.aaq0921 Medline

8. X. Song, Y. Li, X. Cao, Y. Qi, MicroRNAs and their regulatory roles in plant-environment interactions. *Annu. Rev. Plant Biol.* **70**, 489–525 (2019). doi:10.1146/annurev-arplant-050718-100334 Medline

9. I. R. Henderson, X. Zhang, C. Lu, L. Johnson, B. C. Meyers, P. J. Green, S. E. Jacobsen, Dissecting *Arabidopsis* thaliana DICER function in small RNA processing, gene silencing and DNA methylation patterning. *Nat. Genet.* **38**, 721–725 (2006). doi:10.1038/ng1804 Medline

10. Z. Xie, E. Allen, A. Wilken, J. C. Carrington, DICER-LIKE 4 functions in trans-acting small interfering RNA biogenesis and vegetative phase change in *Arabidopsis* thaliana. *Proc. Natl. Acad. Sci. U.S.A.* **102**, 12984–12989 (2005). doi:10.1073/pnas.0506426102 Medline

11. A. Deleris, J. Gallego-Bartolome, J. Bao, K. D. Kasschau, J. C. Carrington, O. Voinnet, Hierarchical action and inhibition of plant Dicer-like proteins in antiviral defense. *Science* **313**, 68–71 (2006). doi:10.1126/science.1128214 Medline

12. H. Wu, B. Li, H. O. Iwakawa, Y. Pan, X. Tang, Q. Ling-Hu, Y. Liu, S. Sheng, L. Feng, H. Zhang, X. Zhang, Z. Tang, X. Xia, J. Zhai, H. Guo, Plant 22-nt

siRNAs mediate translational repression and stress adaptation. *Nature* **581**, 89–93 (2020). doi:10.1038/s41586-020-2231-y Medline

13. R. A. Mosher, F. Schwach, D. Studholme, D. C. Baulcombe, PolIVb influences RNA-directed DNA methylation independently of its role in siRNA biogenesis. *Proc. Natl. Acad. Sci. U.S.A.* **105**, 3145–3150 (2008). doi:10.1073/pnas.0709632105 Medline

14. M. Ronemus, M. W. Vaughn, R. A. Martienssen, MicroRNA-targeted and small interfering RNA-mediated mRNA degradation is regulated by argonaute, dicer, and RNA-dependent RNA polymerase in *Arabidopsis*. *Plant Cell* **18**, 1559–1574 (2006). doi:10.1105/tpc.106.042127 Medline

15. F. Vazquez, H. Vaucheret, R. Rajagopalan, C. Lepers, V. Gasciolli, A. C. Mallory, J.-L. Hilbert, D. P. Bartel, P. Crété, Endogenous trans-acting siRNAs regulate the accumulation of *Arabidopsis* mRNAs. *Mol. Cell* **16**, 69–79 (2004). doi:10.1016/j.molcel.2004.09.028 Medline

16. Z. Xie, L. K. Johansen, A. M. Gustafson, K. D. Kasschau, A. D. Lellis, D. Zilberman, S. E. Jacobsen, J. C. Carrington, Genetic and functional diversification of small RNA pathways in plants. *PLOS Biol.* **2**, E104 (2004). doi:10.1371/journal.pbio.0020104 Medline

17. X. Zhang, I. R. Henderson, C. Lu, P. J. Green, S. E. Jacobsen, Role of RNA polymerase IV in plant small RNA metabolism. *Proc. Natl. Acad. Sci. U.S.A.* **104**, 4536–4541 (2007). doi:10.1073/pnas.0611456104 Medline

18. X. Cao, S. E. Jacobsen, Role of the arabidopsis DRM methyltransferases in de novo DNA methylation and gene silencing. *Curr. Biol.* **12**, 1138–1144 (2002). doi:10.1016/S0960-9822(02)00925-9 Medline

19. C. F. Li, O. Pontes, M. El-Shami, I. R. Henderson, Y. V. Bernatavichute, S. W.-L. Chan, T. Lagrange, C. S. Pikaard, S. E. Jacobsen, An ARGONAUTE4-containing nuclear processing center colocalized with Cajal bodies in *Arabidopsis* thaliana. *Cell* **126**, 93–106 (2006). doi:10.1016/j.cell.2006.05.032 Medline

20. A. T. Wierzbicki, T. S. Ream, J. R. Haag, C. S. Pikaard, RNA polymerase V transcription guides ARGONAUTE4 to chromatin. *Nat. Genet.* **41**, 630–634 (2009). doi:10.1038/ng.365 Medline

21. D. Zilberman, X. Cao, S. E. Jacobsen, ARGONAUTE4 control of locus-specific siRNA accumulation and DNA and histone methylation. *Science* **299**, 716–719 (2003). doi:10.1126/science.1079695 Medline

22. H. Nagano, A. Fukudome, A. Hiraguri, H. Moriyama, T. Fukuhara, Distinct substrate specificities of *Arabidopsis* DCL3 and DCL4. *Nucleic Acids Res.* **42**, 1845–1856 (2014). doi:10.1093/nar/gkt1077 Medline

23. J. Zhai, S. Bischof, H. Wang, S. Feng, T. F. Lee, C. Teng, X. Chen, S. Y. Park, L. Liu, J. Gallego-Bartolome, W. Liu, I. R. Henderson, B. C. Meyers, I. Ausin, S. E. Jacobsen, A one precursor one siRNA model for Pol IV-dependent siRNA biogenesis. *Cell* **163**, 445–455 (2015). doi:10.1016/j.cell.2015.09.032 Medline

24. J. Singh, V. Mishra, F. Wang, H. Y. Huang, C. S. Pikaard, Reaction mechanisms of Pol IV, RDR2, and DCL3 drive RNA channeling in the siRNA-directed DNA methylation pathway. *Mol. Cell* **75**, 576–589.e5 (2019). doi:10.1016/j.molcel.2019.07.008 Medline

25. Y. Qi, A. M. Denli, G. J. Hannon, Biochemical specialization within *Arabidopsis* RNA silencing pathways. *Mol. Cell* **19**, 421–428 (2005). doi:10.1016/j.molcel.2005.06.014 Medline

26. S. Li, L. E. Vandivier, B. Tu, L. Gao, S. Y. Won, S. Li, B. Zheng, B. D. Gregory, X. Chen, Detection of Pol IV/RDR2-dependent transcripts at the genomic scale in *Arabidopsis* reveals features and regulation of siRNA biogenesis. *Genome Res.* **25**, 235–245 (2015). doi:10.1101/gr.182238.114 Medline

27. H. Song, X. Fang, L. Jin, G. X. Shaw, Y.-X. Wang, X. Ji, The Functional cycle of Rnt1p: Five consecutive steps of double-stranded RNA processing by a eukaryotic RNase III. *Structure* **25**, 353–363 (2017). doi:10.1016/j.str.2016.12.013 Medline

28. J. Gan, J. E. Tropea, B. P. Austin, D. L. Court, D. S. Waugh, X. Ji, Structural insight into the mechanism of double-stranded RNA processing by ribonuclease III. *Cell* **124**, 355–366 (2006). doi:10.1016/j.cell.2005.11.034 Medline

29. S. Mi, T. Cai, Y. Hu, Y. Chen, E. Hodges, F. Ni, L. Wu, S. Li, H. Zhou, C. Long, S. Chen, G. J. Hannon, Y. Qi, Sorting of small RNAs into *Arabidopsis* argonaute complexes is directed by the 5′ terminal nucleotide. *Cell* **133**, 116–127 (2008). doi:10.1016/j.cell.2008.02.034 Medline

30. Y. Qi, X. He, X.-J. Wang, O. Kohany, J. Jurka, G. J. Hannon, Distinct catalytic and noncatalytic roles of ARGONAUTE4 in RNA-directed DNA methylation. *Nature* **443**, 1008–1012 (2006). doi:10.1038/nature05198 Medline

31. D. N. Mastronarde, Automated electron microscope tomography using robust prediction of specimen movements. *J. Struct. Biol.* **152**, 36–51 (2005). doi:10.1016/j.jsb.2005.07.007 Medline

32. S. Q. Zheng, E. Palovcak, J.-P. Armache, K. A. Verba, Y. Cheng, D. A. Agard, MotionCor2: Anisotropic correction of beam-induced motion for improved cryo-electron microscopy. *Nat. Methods* **14**, 331–332 (2017). doi:10.1038/nmeth.4193 Medline

33. A. Rohou, N. Grigorieff, CTFFIND4: Fast and accurate defocus estimation from electron micrographs. *J. Struct. Biol.* **192**, 216–221 (2015). doi:10.1016/j.jsb.2015.08.008 Medline

34. S. H. W. Scheres, Amyloid structure determination in RELION-3.1. *Acta Crystallogr. D Struct. Biol.* **76**, 94–101 (2020). doi:10.1107/S2059798319016577 Medline

35. P. Emsley, B. Lohkamp, W. G. Scott, K. Cowtan, Features and development of Coot. *Acta Crystallogr. D Biol. Crystallogr.* **66**, 486–501 (2010). doi:10.1107/S0907444910007493 Medline

36. J. Zivanov, T. Nakane, B. O. Forsberg, D. Kimanius, W. J. H. Hagen, E. Lindahl, S. H. W. Scheres, New tools for automated high-resolution cryo-EM structure determination in RELION-3. *eLife* **7**, e42166 (2018). doi:10.7554/eLife.42166 Medline

37. M. Su, goCTF: Geometrically optimized CTF determination for single-particle cryo-EM. *J. Struct. Biol.* **205**, 22–29 (2019). doi:10.1016/j.jsb.2018.11.012 Medline

38. P. V. Afonine, B. K. Poon, R. J. Read, O. V. Sobolev, T. C. Terwilliger, A. Urzhumtsev, P. D. Adams, Real-space refinement in PHENIX for cryo-EM and crystallography. *Acta Crystallogr. D Struct. Biol.* **74**, 531–544 (2018). doi:10.1107/S2059798318006551 Medline

39. E. F. Pettersen, T. D. Goddard, C. C. Huang, G. S. Couch, D. M. Greenblatt, E. C. Meng, T. E. Ferrin, UCSF Chimera—A visualization system for exploratory research and analysis. *J. Comput. Chem.* **25**, 1605–1612 (2004). doi:10.1002/jcc.20084 Medline

40. S. H. W. Scheres, S. Chen, Prevention of overfitting in cryo-EM structure determination. *Nat. Methods* **9**, 853–854 (2012). doi:10.1038/nmeth.2115 Medline

41. L. Swint-Kruse, C. S. Brown, Resmap: Automated representation of macromolecular interfaces as two-dimensional networks. *Bioinformatics* **21**, 3327–3328 (2005). doi:10.1093/bioinformatics/bti511 Medline

42. B. Langmead, S. L. Salzberg, Fast gapped-read alignment with Bowtie 2. *Nat. Methods* **9**, 357–359 (2012). doi:10.1038/nmeth.1923 Medline

43. A. R. Quinlan, I. M. Hall, BEDTools: A flexible suite of utilities for comparing genomic features. *Bioinformatics* **26**, 841–842 (2010). doi:10.1093/bioinformatics/btq033 Medline

44. A. Kozomara, M. Birgaoanu, S. Griffiths-Jones, miRBase: From microRNA sequences to function. *Nucleic Acids Res.* **47** (D1), D155–D162 (2019). doi:10.1093/nar/gky1141 Medline

45. Y. Z. Tan, P. R. Baldwin, J. H. Davis, J. R. Williamson, C. S. Potter, B. Carragher, D. Lyumkis, Addressing preferred specimen orientation in single-particle cryo-EM through tilting. *Nat. Methods* **14**, 793–796 (2017). doi:10.1038/nmeth.4347 Medline